AerospaceEurope Conference2020
BORDEAUX, FRANCE | 25 - 28 FEBRUARY 2020
CEAS Council of European Aerospace Societies
HOSTED BY : 3AF Association Aéronautique et Astronautique de France

Suction and pulsed blowing for control of local wing-engine-slat-cut out flow separation: The INAFLOWT Project

Monat Shay [(1)], Possti Maayan [(1)], Junaid Ullah [(2)], Yaniv Ariel [(1)], Mizrahi Bar [(1)], Drori Ofek [(1)], Seifert Avraham [(1)]

[(1)] Faculty of Engineering, Tel-Aviv University, Ramat-Aviv 69978, Israel, Email: shaymonat@gmail.com

[(2)] Institute of Aerodynamics and Gas Dynamics, University of Stuttgart, Pfaffenwaldring 21, 70569 Stuttgart, Germany, Email: ullah@iag.uni-stuttgart.de

KEYWORDS: Active Flow control, high lift, local separation, suction, pulsed blowing, High bypass ratio turbofan engine.

ABSTRACT:

An experimental study on the application of active flow control (AFC) to a 1:8.4 scale model of a swept wing in a landing configuration was conducted. The wing is fitted with an Ultra High Bypass Ratio (UHBR) engine nacelle. The highly efficient UHBR engines characterized by a large diameter that interferes with the flow around the wing, degrading its performance. An innovative active flow control device, creating steady suction and pulsed blowing (PB), was installed in the leading-edge region of the wing, above the nacelle, and its performance was experimentally evaluated. The effects of the suction and PB mechanisms were examined individually and simultaneously, using relevant normalized parameters to pave the way to a full-scale wind tunnel test. It was shown that the AFC devices increase the lift by up to 3%, redirected the flow to the desired down-stream direction and reduced the size of the separation zone created due to the implementation of the UHBR nacelle. The next step is validating the small-scale results of this study in full-scale wind tunnel tests that hopefully make the technology flight test ready.

1. INTRODUCTION

The number of commercial flights rises steadily, the impact on the environment becomes more substantial as aircrafts release a considerable amount of greenhouse gasses to the atmosphere, contributing to climate change. One way of reducing aircraft emissions is by installing a more fuel-efficient engine such as the Ultra High Bypass Ratio (UHBR) turbofan [1]. This engine includes a significantly larger diameter fan relative to the engine core, which maximizes the mass flow around the core with minimal speed increment, thus reducing the thrust specific fuel consumption while increasing the overall diameter of the nacelle. Incorporating this larger diameter engine in a typical airliner poses an engineering challenge [2]. The engine is to be mounted under the wing, to reduce cabin noise, thereby its size is limited by the minimal safe ground clearance below, and by the wing above. The solution for this challenge, with the current length of the landing gear, is to mount the engine closer to the wing, with the slats cut wider away from the pylon to avoid clashing with the nacelle.

The close coupling of the nacelle, wing and slat complicates the flow and creates structures that significantly alter the direction and near-wall momentum of the flow, leading to local separations, reduced lift and increased drag [3–5]. As part of several European-Union-funded studies, the effects of this close coupling have been examined in several wind tunnel experiments [3, 5, 6] and Computational Fluid Dynamics (CFD) simulations [3, 7–9]. These studies show that the main harmful effects can be traced to a region downstream of the nacelle, between the inboard side of the pylon and the slats, where the flow is reversed (marked blue in Figure 1), and longitudinal vortices are prominent (Figure 2). Thus, to incorporate the UHBR engines in new commercial aircraft, a method to redirect and re-energize the near-wall flow is needed.

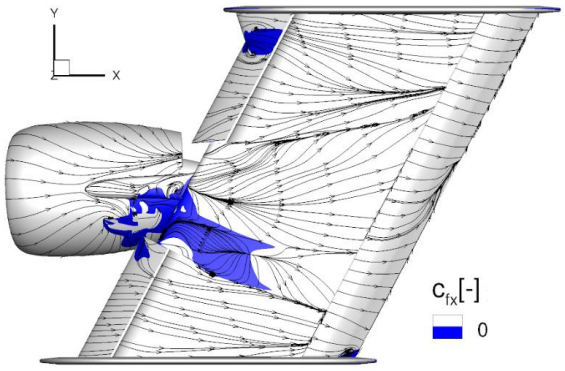

Figure 1. CFD simulation of wing-nacelle junction showing flow separation regions in blue. The targeted region is inboard of the nacelle [3].

To deal with the local flow separation described above, a passive flow control solution in the form of a strake was positioned on the nacelle [6, 10]. However, this solution is insufficiently effective [6]. Therefore, the current solution is for Active Flow Control (AFC) devices [11], creating periodic excitation [12, 13]. Periodic excitation has been shown in the past as a plausible flow control mechanism for increasing lift, stall postponement, controlling complex flow structures and even acting as virtual control surfaces [13–15]. Conveniently, the leading edge (LE) of the disturbed area can house these devices where slats do not exist

directly downstream of the pylon. The implementation of AFC devices in the wing-pylon junction has been examined in past efforts as part of the EU AFLoNext project [16], where pulsed jet actuators (PJA) and Synthetic Jet Actuators (SJA) were simulated, installed [17] and tested. These tests showed promising results, but the high mass flow consumption (of PJA) and the insufficient momentum provided (by the SJA), call for a different device to be used.

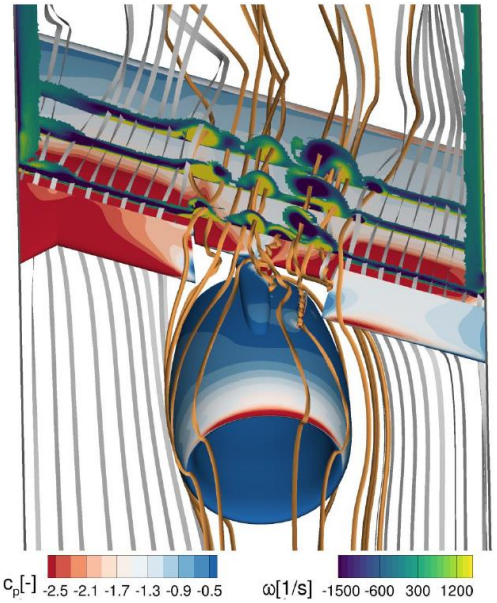

Figure 2. CFD simulation of the longitudinal vortices formed by the geometry of the slat edges, strake and nacelle [9].

Within the scope of the EU TAU lead INAFLOWT project [18, 19], an innovative AFC device in the form of Suction and Oscillatory Blowing (SaOB) actuator is used to alleviate the local boundary layer separation caused by the UHBR installment. The SaOB actuator (Figure 3), developed at Tel-Aviv University, is a fluidic device that consists of two main elements; the ejector which is creating the steady suction and the oscillator (by-stable fluidic amplifier) which is responsible for the oscillatory blowing flow. Its principle of operation and performance has been extensively studied [20, 21].

This paper presents the experimental study conducted on a small-scale model of a wing segment with a UHBR nacelle at Tel Aviv University's Knapp-Meadow low-speed wind tunnel. SaOB actuators were adapted to fit into the small-scale model, their performance was evaluated, and they were installed in the model for a series of wind tunnel tests. The conducted tests covered a range of free-stream velocities, angles of attack (AoA) and actuation magnitudes. Wind tunnel test data was collected to assess the change in pressure distributions, integrated lift and the development of streamwise vortices in the near wake. This study was conducted along with CFD simulations by the INAFLOWT project partners from VZLU [21], University of Stuttgart (USTUTT) [3] and Israel Aerospace Industry (IAI).

The goal of this study is to verify that the SaOB actuator is capable to re-energize, redirect the flow and to recover the lift loss due to the geometry dictated by the UHBR nacelle, in preparation of a near-full-scale wind tunnel test to be conducted in the Central Aerohydrodynamic Institute (TsAGI) in Zhukovskiy, Russia.

The structure of the paper is as follows: section 2 will present the experimental setup; first by describing the wind tunnel, wing test model and AFC devices. Section 2 will also describe the sensors and equipment used in the tests. Section 3 will cover the actuators' bench-top test results, a parametrized discussion of the wind tunnel test results and an analysis of the near wake of the model. Conclusions and future directions will be discussed in section 4.

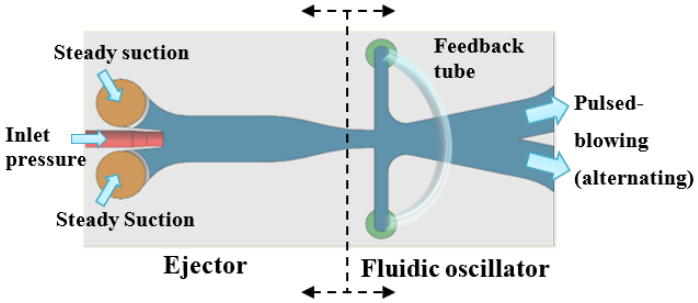

Figure 3. A sketch of a SaOB device, parts and operation principle [22].

2. EXPERIMENTAL SETUP

2.1. Small Scale Model

Figure 4. The LSM (termed also BFM) at the T-101 WT in TsAGI during the INAFLOWT project. The span and the chord of this model are larger than 5m.

In continuation to previous studies on the specific geometry of swept-wing with UHBR nacelle, the current study uses a scaled-down version of the large-scale model (LSM) (Figure 4) that was wind-tunnel tested at the closed-loop subsonic wind tunnel T-101 at TsAGI [23–25] as part of the AFLoNext project. The current model is scaled down by a factor of 1:8.4, to fit inside the Knapp-

Meadow WT with the end-plates of the LSM removed so it spans the entire width of the WT. Similarly to the LSM, the small-scale model (SSM) has a 28° backward-swept wing LE based on the DLR-F15 airfoil [26], with flap and slat deflected at 35° and -28°, respectively, representing a landing configuration. The pylon and nacelle are mounted at the mid-span of the wing with the slats on both sides of the nacelle. The nacelle is a hollow outer shell of an UHBR engine with only the hollow core of the engine inside it and a strake outside, on the inboard side of the nacelle (shown in Figure 5).

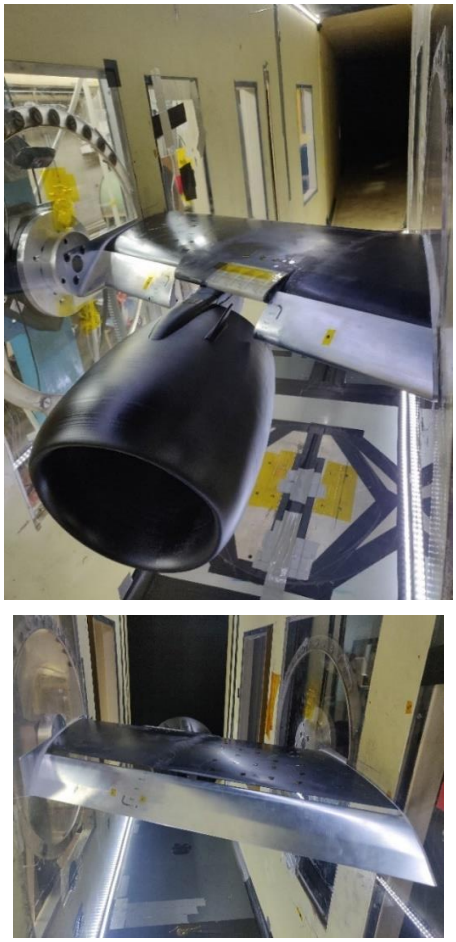

Figure 5. Front (top) and rear (bottom) views of the SSM (or GSM) installed at the TAU Knapp-Meadow WT at TAU.

The span of the model is 608 [mm] and its chord, including the flap and slats, is 430 [mm], measured normal to the LE. However, due to considerations of the INAFLOWT project, the chord length for calculations is 387 [mm]. The maximum diameter of the nacelle is 236 [mm] and its core diameter is 110 [mm]. The test-section of the Knapp-Meadow wind tunnel at Tel Aviv University is 608 [mm] wide, 1500 [mm] high and 4250 [mm] in length. The tunnel blockage ratio of the model (at AoA = 0°) is 7.6%. The model's rotation axis is positioned 1250 [mm] downstream from the entrance to the test section at mid-height. The model is installed between two, 480 [mm] diameter, plexiglass discs which act as the rotation axis (Figure 5). The main element of the SSM was fabricated from a 5 [mm] thick shell of fiberglass-epoxy, the flap and slats were made of CNC-machined aluminum and the nacelle with its core and pylon were 3D printed from PLA material, assembled from a few parts, polished and painted.

The lift generated by the wing was evaluated by integrating the pressures along two sections in the wing, flap and slats. These inboard (55 pressure taps) and outboard (69 pressure taps) sections are seen in red and green, respectively, in Figure 6, along with the forward (14 pressure taps) and aft (11 pressure taps) spanwise rows of pressure taps, marked by blue and yellow lines, respectively. Several additional pressure taps are located between the actuators and in other key locations in the separated flow region, counting a total of 159 pressure taps on the surface of the wing. The inner cavity of the wing could be accessed by removing a cover plate at the bottom of the wing.

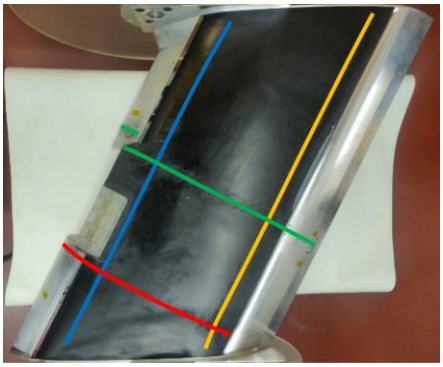

Figure 6. A top view of the SSM (nacelle removed) showing the pressure taps sections. Inboard and outboard chordwise sections are marked by red and green lines, respectively. Forward and aft spanwise rows are blue and yellow lines, respectively.

2.2. The AFC array module

Incorporating the SaOB devices in the SSM posed several challenges, due to the small volume of the LE segment above and inboard of the nacelle, where AFC is required (Figure 7). Ultimately, it was decided to fit 4 fluidic oscillators and 8 corresponding suction holes in this volume. The AFC array module is a single, 3D printed block, manufactured using an advanced SLA printer with a printing layer resolution of 25 [µm]. It was also decided that the suction and fluidic oscillator of each actuator will be two independent mechanisms, thus allowing flexibility to control the steady suction and pulsed blowing (PB) independently at different actuation magnitudes, unlike in the conventional SaOB actuator where they are coupled. This de-coupling allows us to study the optimal relation between suction and PB, and support the design of the full-scale SaOB device, which will be used in the next step of the INAFLOWT project, outside the scope of this paper.

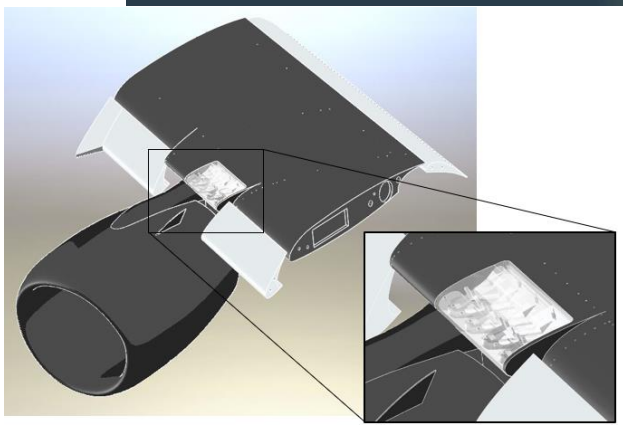

Figure 7. A CAD Image of the SSM with the AFC array module in the LE above the nacelle.

The steady suction effect is created by 8 suction holes, shaped as 2 [mm] by 3 [mm] oval slots, major axis parallel to the LE, evenly spaced along the 0.014 [x/c] chord location between the inboard slat and the pylon. Each pair of suction holes corresponds to a fluidic oscillator, situated between the pair, as can be seen in Figure 8, simulating a regular SaOB configuration. The fluidic oscillators are facing down-stream, normal to the leading edge, with their exit slots located along the 0.125 [x/c] chord location and ejecting the PB jets at a shallow angle relative to the surface of the wing in the downstream direction.

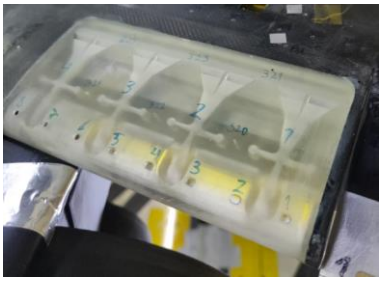

Figure 8. The SLA 3D-printed AFC array module integrated into the LE of the SSM. The 4 fluidic oscillators and 8 oval suction holes are shown numbered.

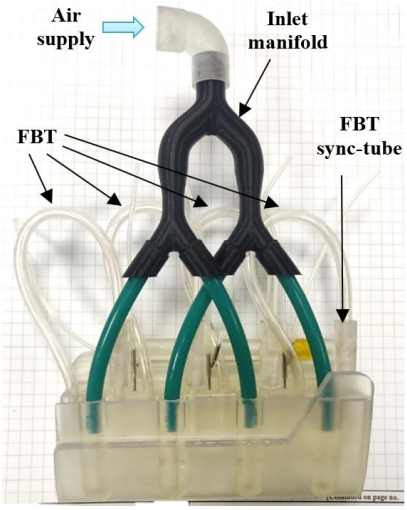

Figure 9. The AFC module with the inlet manifold, FBTs, FBT sync-tube and pressure-taps tubes.

As mentioned, the two AFC mechanisms are adjustable separately. The fluidic oscillators inlet-port can be supplied with compressed air using a mass-flow controller located outside the WT. The inlet air is routed into the wing through the side of the model into a manifold, spreading the flow evenly to the actuators' 4 inlet ports. The suction holes are open to the inner cavity of the wing, where low pressure can be applied using an external pump. The suction cavity pressure was measured during the bench-top tests, and therefore the suction velocity is known.

The 4 fluidic oscillators are operated at identical phases relative to each other, meaning that when one slot of an oscillator is blowing, all slots on the same side will blow, creating synchronized oscillation. The fluidic oscillator periodic behavior is created by the feedback tube (FBT) (seen in Figure 3 and Figure 9), by connecting the feedback tubes of the oscillators, using a synchronization tube (termed sync-tube), the oscillators operate "in-phase". The frequency of the oscillators is measured by an unsteady pressure sensor installed in the sync-tube.

PB and suction velocity measurements were conducted using a hot-wire (HW) probe mounted on a motorized computer-controlled traverse system capable of moving in 3 dimensions. The probe was calibrated by positioning it in the potential core of a calibration jet with a diameter of 20 [mm]. The hot-wire's voltage is measured in a series of points, covering all the relevant velocity range. At each point, the measured voltage is correlated with the jet's velocity, eventually fitting a third-order Polynomial. An overall velocity uncertainty of less than 5% is achieved at low speeds and 2% at speeds above 10 [m/s].

Prior to its installment in the wing, the AFC array module was fixed to a test-bench setup to assess the PB mechanism performance. The air velocity at the exit slots was measured using a hot-wire probe (Figure 10.b.). A Y-coordinate (spanwise) velocity scan (termed Y-scan) of the PB slots was conducted by moving the HW along the row of slots using a motorized, computer-controlled, traverse system. After this scan, the HW was positioned in the location where peak velocity was detected, at each slot, and the air-velocity for a range of inlet pressures was measured at this location (termed P-scan). These tests were repeated for 4, 3, and 2 of the most inboard actuators so the effectiveness of a different number of actuators can be assessed. To create and test arrays of 4, 3, and 2 actuators, the inlet-tube and the FBT were disconnected and the sync-tube was adapted to connect only between active actuators. Although the suction mechanism is separate from the PB mechanism, throughout the WT tests, whenever a fluidic oscillator was disconnected the corresponding pair of suction

holes were taped over as well, to closely mimic SaOB operation.

The AFC module was glued in place at the LE of the wing, using epoxy resin, and polished to create a seamless surface. The interior of the wing was then sealed completely, apart from the 8 (or 6 or 4) suction holes in the AFC module enabling suction.

To measure the suction air velocity, the entire wing model (nacelle removed) was fixed to a test-bench and a HW probe was carefully positioned at the suction holes center at the surface elevation (Figure 10.a.). The suction air velocity was measured for a range of suction pressures and distances from the surface to assess the sensitivity of the measurement to the placement of the probe, found to be very high.

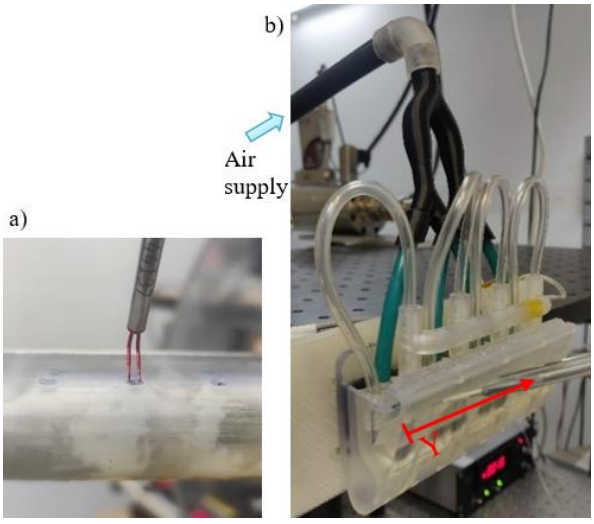

Figure 10. Bench-top tests of the AFC array module using a HW probe. a) HW probe placement in one of the 8 suction holes and b) PB mechanism measurements.

2.3. Near wake measurements

The air-velocity vectors and vortex flow-field in the wake of the model were calculated from the measurements of an array of 4, seven-holes probes (7HP). These probes calculate the wind velocity vector by correlating the pressures measured by the seven holes in its conical tip (Figure 11) as described in-depth in [27]. The probes were calibrated using the rapid calibration method described in [28], where a calibration matrix was created to translate the pressures reading to an air-velocity vector (as described in depth in [29]). The probes are mounted on a traverse system connected to two stepper motors capable of moving the probes in two axes, scanning a 2D (Y-Z) surface normal to the free-stream direction. The tip of the probes was located 1350 [mm] (approximately 3.5 [x/c]) from the model's AoA rotation axes (Figure 12). With these two axes of motion, the velocity vectors and vorticity of almost the entire wind tunnel cross-section can be measured and velocity vectors calculated.

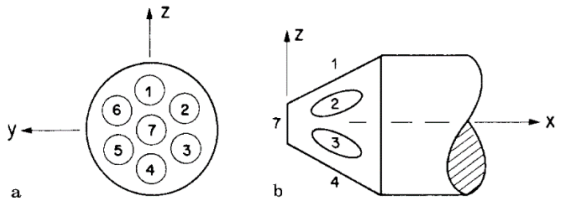

Figure 11. Front view (a) and side view (b) of a Seven-Holes Probe with the ports numbered and principle axes marked [27]. The inner diameter of a single hole is 0.6 [mm] and the diameter of the entire probe is 4 [mm].

Figure 12. Four, Seven-Holes Probes mounted on the wake traverse system, 1350 [mm] downstream from the wing rotation axis and spaced 9 and 12 [cm] apart.

3. RESULTS AND DISCUSSION

3.1. AFC module array bench-top tests

In this section of the paper, we describe the results of the actuator module calibration in otherwise still air. First, a Y coordinate (visible in Figure 10.b.) hot-wire scan was performed at the PB exit slots using a single HW. The HW probe was carefully positioned so it will traverse along the Y-coordinate at a constant distance from the surface and the PB slots of the AFC array module. This is crucial to assure an accurate measurement verifying symmetrical behavior for each actuator.

The results shown in Figure 13 display symmetrical behavior for the blowing velocity of all 4 actuators. The 8 peaks shown in Figure 13 correspond to the 8 blowing slots of the actuators, where the mean velocity (blue rhombus, left-side ordinate) is almost uniform across each slot, peaking close to the splitter. The standard deviation (STD) of the air velocity (red squares, left-side ordinate) is used as an indication of the switching quality (SQ) of the actuators (green triangles, right-scale ordinate). The SQ indicates the quality of the oscillations is simply defined as the ratio between the mean and STD velocities and it indicates if the flow fully switches sides from one slot to the other [22]. The SQ of all 4 actuators is above 0.5 and at places reaches 0.7, which is the SQ of a pure sine wave (between 0 and 2), indicating near-full switching between the two exit slots of each actuator as it oscillates.

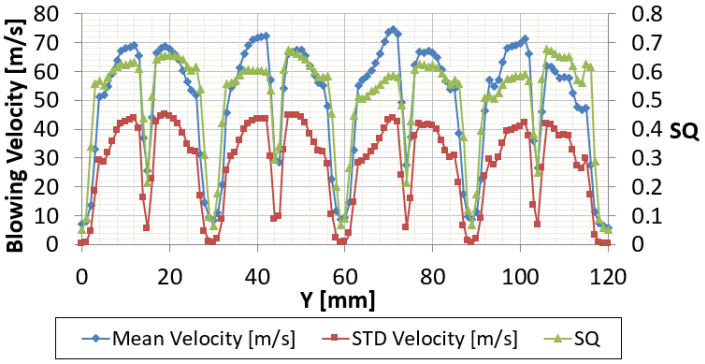

Figure 13. Y coordinate velocity scan at the PB exit slots, using inlet pressure of 69 [kPag]. Mean and standard deviation (STD) velocity of the PB slots is left-side ordinate, switching quality (SQ) is right-side ordinate.

Inlet pressure scans (P-scan) were conducted by positioning the HW in the point where peak velocity was measured in one of the slots in the Y-scans, as shown in Figure 13. Note that this procedure requires careful positioning of the probe near the slot, as the velocity changes significantly at different distances from the slot. This means that relocating the probe in the exact peak-velocity point is inherently prone to uncertainty. Figure 14 shows the blowing velocity vs. the mass flux through one fluidic oscillator for an AFC array of 2, 3, and 4 of the inboard actuators. A maximum velocity of 100 [m/s] was reached. The P-scan measurements produce an important correlation between the inlet pressure, P_{in}, and the PB velocity, as the latter cannot be measured in real-time during the wind tunnel tests.

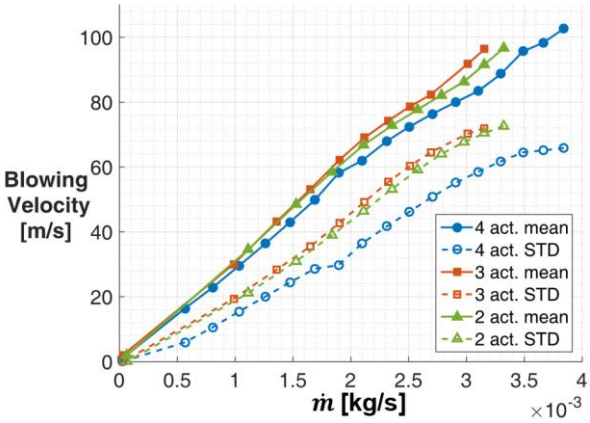

Figure 14. Mean and STD pulsed blowing velocity vs. the mass flow rate through one fluidic oscillator for an AFC array of 2, 3, and 4 inboard actuators. Measured by HW in the peak velocity point in a single slot.

The PB frequency is also important for calculating the nondimensional Strouhal number, F^+, common between different scales and speeds, or identify any unsteady behaviors in the flow and correlate it to past tests and specific unsteady structures. Analyzing the frequency measured with the HW probe (and the FBT pressure signal) during a P-scan provides the relation seen in Figure 15. The frequency measured with the unsteady pressure sensor inside the FBT was identical to the HW probe measurements as seen in Figure 15. The excitation frequencies were chosen to fit $F^+ \approx 1$, which is very receptive in flow control applications. The data from the P-scan measurements also show a linear correlation between the PB frequency and velocity.

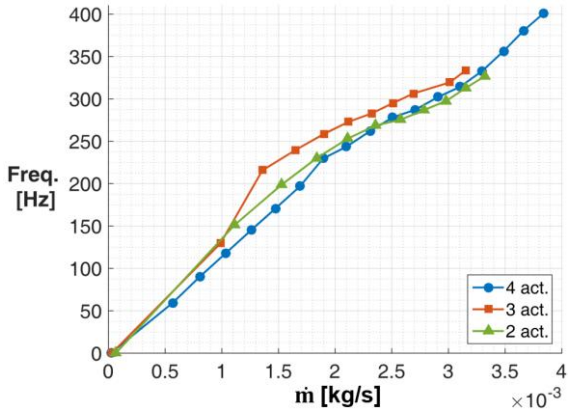

Figure 15. Pulsed blowing frequency vs. the mass flow rate through one fluidic oscillator in AFC arrays of 2, 3, and 4 inboard actuators, measured by HW in the peak velocity point in a single slot.

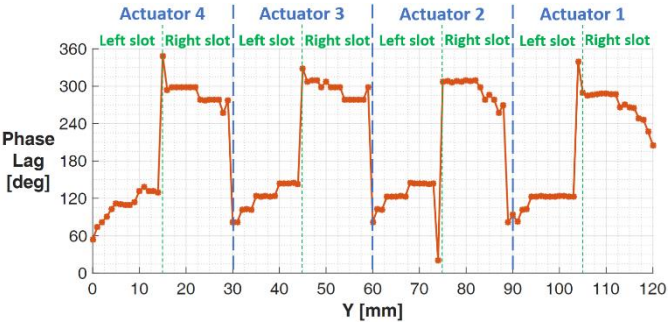

Figure 16. The phase lag between the PB signal measured with the HW probe and the unsteady pressure sensor measured in the FBT with respect to the Y coordinate. Measured while using 4 actuators and mass flux of 0.01 [kg/s]. The measured frequency is 278 [Hz].

It is also important to quantify the phase in which each actuator slot operates when analyzing WT measurements. Since it is not possible to conduct intrusive HW measurements in the WT, we can use the unsteady pressure sensor in the FBT and add the phase lag between it and the PB slots at the surface of the wing. We obtain this phase lag by calculating the phase lag between the unsteady pressure sensor and the HW probe, measured during the bench-top tests. The phase lag calculated during a Y-scan of 4 actuators is shown in Figure 16, showing the approximately 180 [deg] phase between each slot pair of each actuator and a phase variation of 30-60° along a given slot.

The results of the suction holes velocity scans with the probe positioned accurately at the surface of the holes are presented in Figure 17.a. The data shows a maximum air velocity of nearly 120 [m/s] at a suction pressure of -8.6 [kPag], which is the

maximum suction pressure available in the bench-top tests. It was shown during suction holes measurements that the measured velocity decreases by about 8% for every 0.1 [mm] the HW probe is pulled away from the surface. Moreover, in the WT tests, it is possible to reach a suction pressure of up to -10.3 [kPag]. To evaluate the suction-velocity at higher suction pressures, a linear fit was created for the suction-velocity dynamic-pressure vs. the suction pressure (Figure 17.b.). This linear fit was used to predict the dynamic pressure at suction pressures higher than the maximum measured in the bench-top tests and to obtain the suction-velocity estimation at the maximum suction pressure of -10.3 [kPag], used in subsequent WT tests.

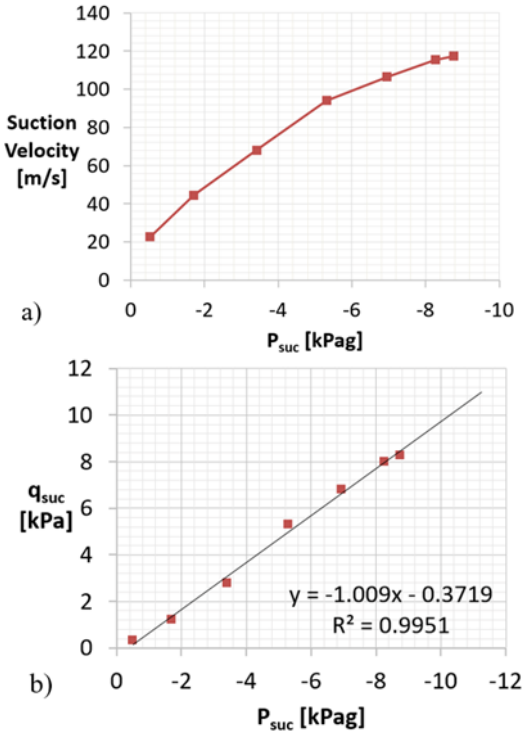

Figure 17. Suction hole HW air-velocity measurements presented as a) HW velocity vs. wing cavity suction pressure and b) dynamic pressure based on HW velocity vs. wing cavity suction pressure with a linear trend-line and best-fitted equation.

3.2. Pressure distribution and integrated Lift

The actuation magnitudes of the AFC array are presented in the parametric none-dimensional form of momentum coefficient, C_μ, and mass-flow coefficient, C_q. The suction magnitude is indicated in the form of momentum coefficient, C_μ, defined by Seifert [13]:

$$C_\mu = \frac{2\rho_s U_s^2 A_s}{\rho_\infty U_\infty^2 A_r} \qquad (1)$$

Where ρ_s is the air density, U_s is the suction air velocity, ρ_∞ and U_∞ are the free-stream density and flow, respectively, A_s is the suction holes cross-section area and A_r is the reference area of the model. It is assumed that for suction $\rho_s = \rho_\infty$.

Since we have direct measurements of the mass-flow to the fluidic oscillator, the momentum coefficient for PB will be calculated as such:

$$C_{\mu_{PB}} = \frac{2\dot{m}U_{PB}}{\rho_\infty U_\infty^2 A_r} \qquad (2)$$

Where $\dot{m}$ is the mass flux through one actuator and U_{PB} is the mean blowing velocity as shown in Figure 14, measured by HW during the bench-top calibration stage. However, in this study we use the mass flux of air through the actuators to quantify the efficiency of the system, thus the actuation magnitude of the PB mechanism is presented by the mass-flow coefficient, defined in [11]:

$$C_q = \frac{\dot{m}}{\rho_\infty U_\infty A_r} \qquad (3)$$

The relation between $C_{\mu,PB}$ and C_q is shown in Figure 18:

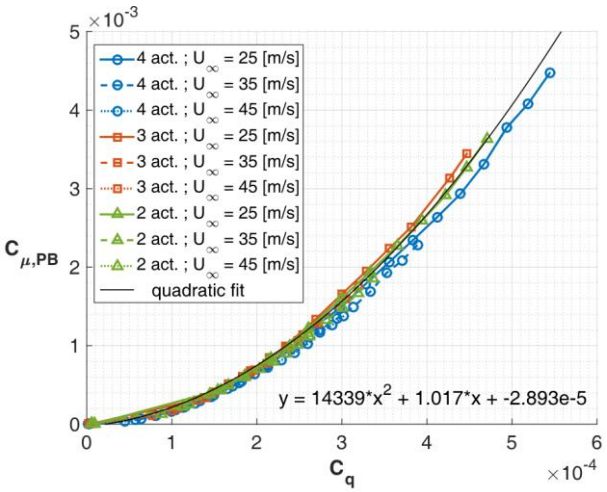

Figure 18. The momentum coefficient of PB, $C_{\mu,PB}$ vs. the mass-flow coefficient, C_q. For a range of free-stream velocities and AFC arrays of 2, 3, and 4 inboard actuators and a quadratic fit of the data.

The main interest of this study is to recover the lift lost due to the implementation of the new wing-pylon-nacelle geometry, therefore measuring the change in the lift is a key topic of this study. By integrating the pressures along the inboard and outboard pressure tap sections (Figure 6) it was possible to receive an estimate of the sectional lift coefficient. Note that the two sections are perpendicular to the LE of the wing and thus angled by 28° relative to the free-stream direction. The measured C_p distributions are shown in Figure 19. Data is presented for the inboard (left) and outboard (right) sections for the baseline case and an actuated case. The data of Figure 19 shows changes in C_p in the flap of the outboard section and slight changes in the trailing edge of the inboard slat and the main element of the outboard section. This data shows that the effects of the

actuators are sensed mostly directly downstream of the actuators and in its immediate surroundings.

Due to scaling effects, wall effects, 3D effects, pressure tap distribution and other limitations, the C_p integrated lift coefficient cannot be used to calculate the overall lift of the wing, but mainly to track local changes in the sectioned lift due to the applied AFC. Studying the results of several WT tests, it was soon established that the outboard row of pressure taps is more sensitive to changes in flow features due to actuation than the inboard section, mainly because the outboard section is partially directly downstream of the actuators. Therefore, it was decided to use the outboard section as the main reference for C_L and ΔC_L evaluation, while using the inboard section was left mostly for trends validation.

During the WT tests, using a free-stream velocity U_∞=25 [m/s], a baseline case where all AFC cavities are taped-over was first measured. The baseline C_L vs. AoA results, shown by a dashed black line in Figure 20, displays a distinct linear lift curve up to 9° AoA, after which separation begins, achieving max-C_L at 11° AoA and stalling at 12° AoA. Next, a suction scan was conducted with the PB slots still taped over. This set of measurements is presented along with the baseline results (Figure 20, left) and with the change in lift, ΔC_L, relative to the taped baseline measurement (Figure 20, right).

As expected, the no-actuation case with AFC cavities open (dashed blue line, Figure 20) is detrimental for lift, since this case simply adds holes near the LE, disrupting the flow and causing premature separation. However, activating the lowest magnitude of suction alleviates the disruptive effects of the suction holes. As the suction magnitude is increased it helps maintain the linear curve up to 10° AoA. Examining the change in the lift it is indicated that suction has a clear and consistent effect on the lift, increasing it by up to 2.5% ($\Delta C_L \approx 0.05$), whereas further increasing the suction pressure, it seems to saturate at $C\mu = 9.2\times10^{-3}$.

The effects of steady suction and PB were examined by using each method separately and then simultaneously. The lift and lift increment shown for 35 [m/s] free-stream velocity in Figure , demonstrate the same behavior for baseline cases as seen for 25 [m/s] (Figure 20). The baseline lift slightly degrades as the suction holes and PB slots are exposed. When no mass flux is introduced into the fluidic oscillators and using only a suction pressure yielding $C_\mu = 2.5\times10^{-3}$ (continuous blue line and triangles in Figure), the sectional lift coefficient is increased substantially, peaking at 11° AoA. At AoAs higher than 11° the effect of suction diminishes until failing at the stall angle of 12° AoA. When introducing PB alone (green line and rectangles in Figure) with an actuation

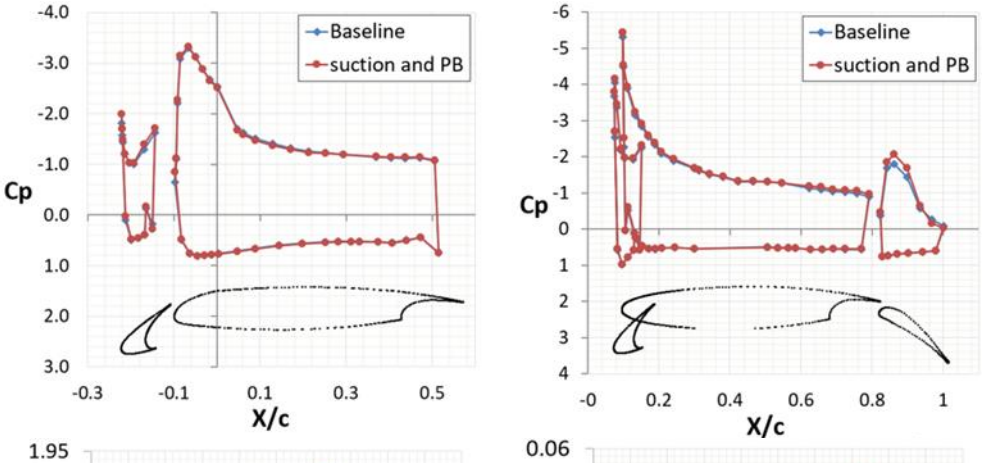

Figure 19. Cp distributions in the chordwise direction along with an outline of the wing section in black for inboard (left) and outboard (right) sections. At free-stream velocity of U_∞ = 45 [m/s] ($Re = 1.1\times10^6$) for the baseline flow and using 8 suction holes to create suction momentum coefficient of $C_\mu = 2.2\times10^{-3}$ and 4 fluidic oscillators to create PB with a mass flow coefficient of $C_q = 2.8\times10^{-4}$.

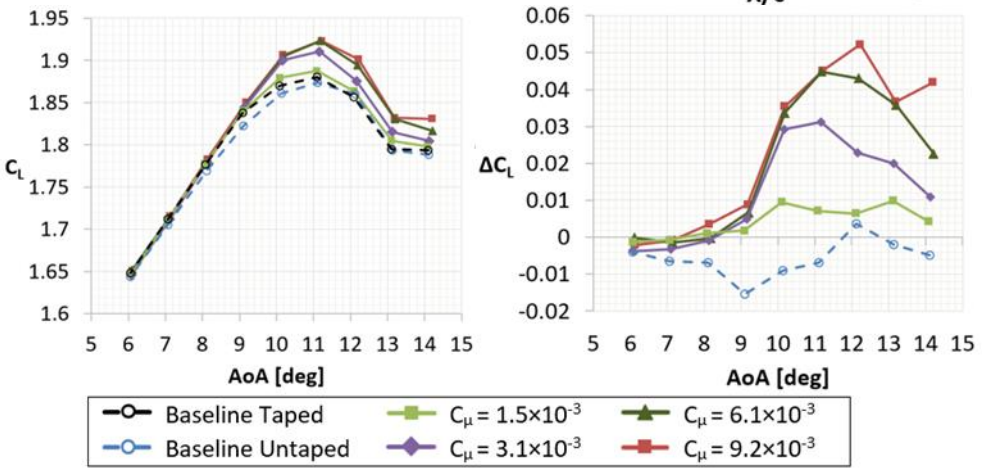

Figure 20. Sectional lift coefficient, C_L, (left) and the change in lift, ΔC_L, (right) with respect to AoA (ΔC_L calculated relative to the taped baseline case) with steady suction applied from 8 suction holes and PB slots taped. At U_∞ = 25 [m/s] ($Re = 6.4\times10^5$). ΔC_L calculated relative to the taped baseline case.

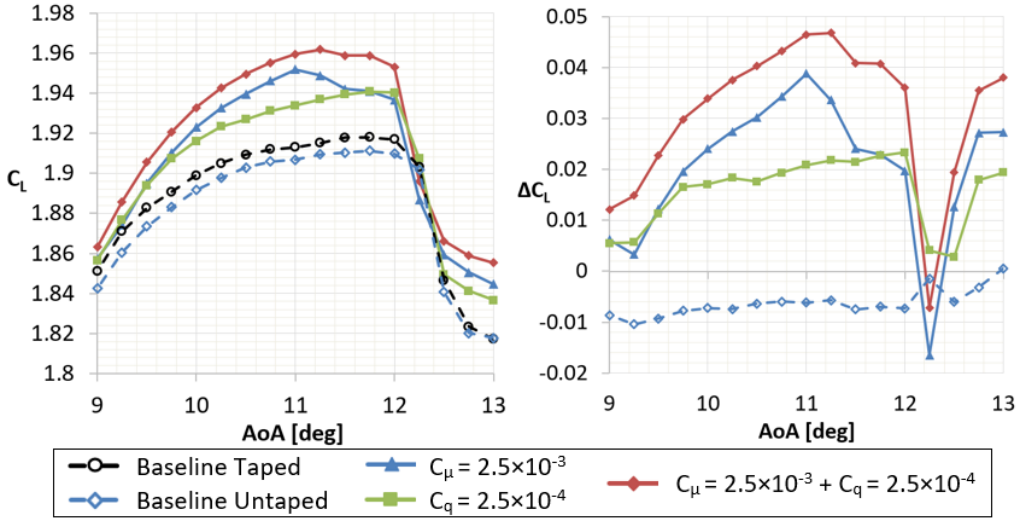

Figure 21. Sectional lift coefficient, C_L, (left) and the change in lift, ΔC_L, (right) with respect to AoA using both AFC methods separately and Combined. At U_∞ = 35 [m/s] (Re = 9.0×10^5) while using 6 suction holes and 3 fluidic oscillators. ΔC_L calculated relative to the taped baseline case.

magnitude yielding $C_q = 2.5\times10^{-4}$ it is apparent that it maintains a steady increase in the lift for AoAs between 10° and 12° (stall angle). Interestingly, when examining the PB with suction case relative to the suction alone case (red line relative to blue line in Figure), it is apparent that adding PB to suction has a stronger contribution to C_L, compared to each mechanism separately, between 11°-12° AoA rather than at AoAs lower than 11°.

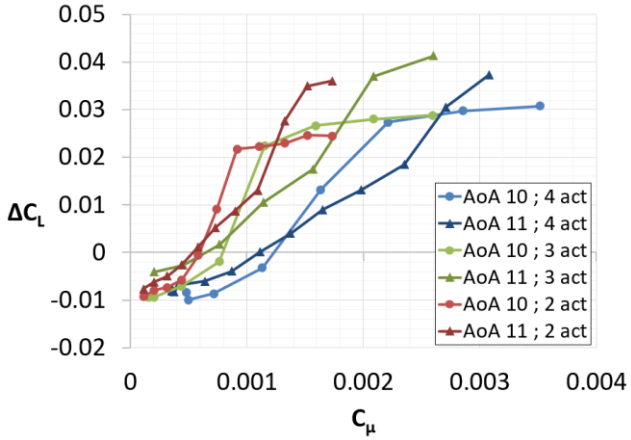

Figure 22.The change in lift, ΔC_L, for a suction pressure scan performed at U_∞ = 45 [m/s] (Re = 1.1×10^6). Data acquired at 10° and 11° AoA while using 2, 3 or 4 inboard actuators (4-8 suction holes).

During the experiments at U_∞ = 45 [m/s], the effects of a different number of actuators on the lift were measured at 10° and 11° AoA. In each case, the most outboard actuator(s) were disabled by disconnecting the fluidic oscillator from the inlet manifold and taping over its corresponding suction holes and PB slots. Figure 22. shows the change in the lift as affected by the suction momentum coefficient, calculated using Eq. (1). These results show that the 3 actuators case reaches a slightly higher ΔC_L than the 2 actuators case, albeit using a higher C_μ. Whereas the 4 actuators case improves the lift slightly less than the 3 actuators case even when a much higher C_μ per actuator is used. This data allows us to conclude that for suction alone, the 3 most inboard actuators suffice.

To assess the effectiveness of a different number of fluidic oscillators, the PB magnitude was scanned for 2, 3 and 4 actuators while using a constant suction pressure of -7.9 [kPag] (C_μ = 1.2×10^{-3}, 1.7×10^{-3}, 2.4×10^{-3} for 2, 3, and 4 actuators, respectively). The mean nozzle-air-velocity is derived using the data of Figure 14 and is referenced to the free-stream velocity by the Velocity-Ratio (VR) which is a quotient of the two. The lift variation, ΔC_L, of the PB scan (with constant suction magnitude) is presented vs. the

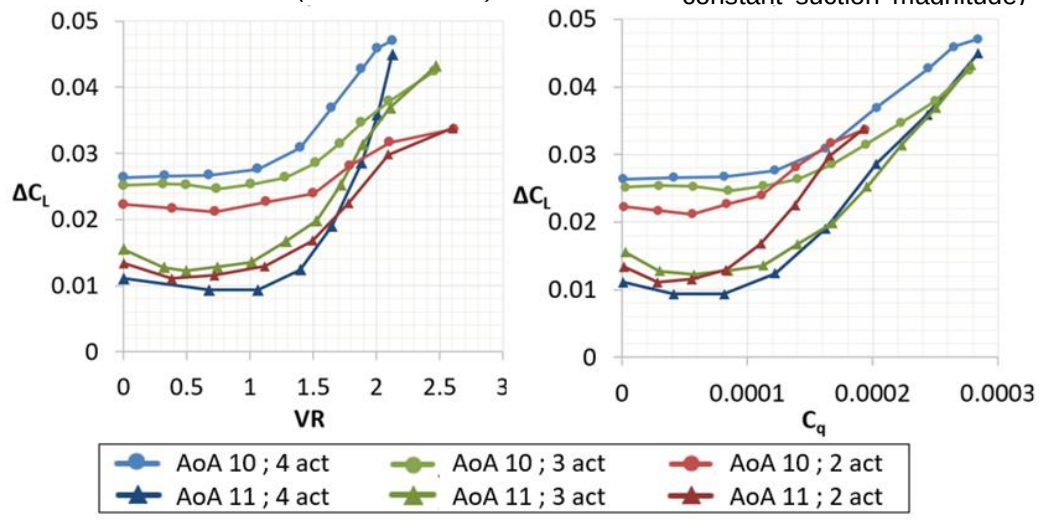

Figure 21. The change in lift, ΔC_L, with respect to the relative PB velocity, VR, (left) and with respect to the PB mass flow coefficient, C_q, of a single actuator (right). Using 2-4 actuators at 10° and 11° AoA and a constant suction pressure of -7.9 [kPag] ($C_\mu = 1.2\times10^{-3}$, 1.7×10^{-3}, 2.4×10^{-3} for 2, 3, and 4 actuators, respectively). U_∞ = 45 [m/s] (Re = 1.1×10^6).

PB VR in Figure 23, left. It is demonstrated that up to VR = 1.5 the PB has no added effect on the lift, but for higher VR the lift increases significantly. As expected, the more actuators, the better the lift increment for the same relative PB velocity. However, adding more actuators means that a higher mass flux is needed. Presenting the same data versus the mass flow coefficient, C_q, of the actuators (Figure 23, right) shows that the efficiency of the 3 actuators case is higher in terms of the invested mass flux. It is evident that the 3 actuators case reaches almost the same lift as the 4 actuators case for a substantially lower mass flux. Clearly, the contribution of the 4th actuator is much lower than the 3rd actuator (in addition to the 2 most inboard actuators).

3.3. Near wake scans

3.3.1. Drag estimation from wake velocity scans

Once the air-velocity 3D vectors and pressures were obtained for the 2D surface in the wake of the model, an assessment of the drag coefficient can be made. By using the equation to calculate drag from wake measurement derived by van Dam [30] and subtracting from it the thrust created by the AFC mechanisms, we arrive at eq. (4):

$$D = -\dot{m}_{PB}U_\infty + A_{suc}p_{suc} + \iint_{wake} [\rho u(U_\infty - u) + (p_\infty - p)]\, dS \quad (4)$$

Eq. (4) includes the Betz correction which considers the pressure gradient in the wake. An alternative form for this formula is suggested by Giles and Cummings [31] where the Betz correction is replaced by air-velocity components in the wake, normal to the free stream direction:

$$D = -\dot{m}_{PB}U_\infty + A_{suc}p_{suc} + \iint_{wake} \left[\rho u(U_\infty - u) + \frac{1}{2}\rho(v^2 + w^2)\right] dS \quad (5)$$

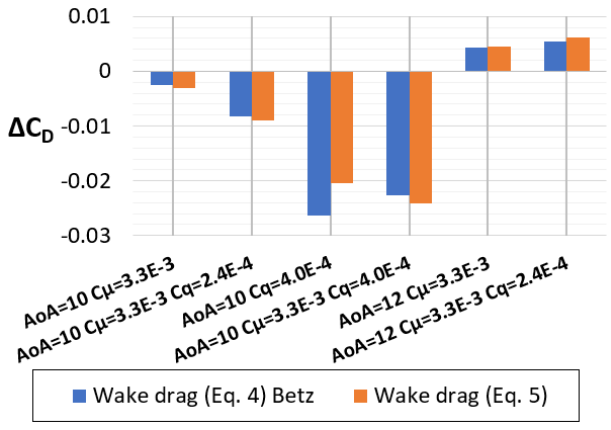

Figure 23. The change in drag coefficient, ΔC_D, for 10° and 12° AoA and several AFC actuation magnitudes at U_∞ = 25 [m/s] (Re = 6.4×10⁵).

Since wake measurements are time-consuming, only a handful of measurements were made. By using both equations (4) and (5) and subtracting the baseline case, we obtain the change in drag coefficient, ΔC_D, presented in Figure 23. From this data it appears that at 10° AoA applying AFC is beneficial to drag reduction, reaching about 20% when PB actuation magnitude is increased to C_q = 4.0×10⁻⁴ (or VR = 3). However, at 12° AoA (stall angle) AFC does not lead to drag reduction. The agreement between the two drag estimation methods is ±0.003 of the mean ΔC_D.

3.3.2. Longitudinal vortices

To investigate the creation and development of longitudinal vortices, the spanwise pressure distribution on the wing is examined together with the velocity vectors and streamwise vorticity in the wake of the model. The two are linked by Helmholtz's 2nd theorem and Prandtl's lifting line theory. Figure 25 presents the vortex field (color map) overlaid by the velocity vectors field (small blue arrows) of the Z-Y plane at the wake of the model, and below these, sharing the same horizontal axis, are the spanwise pressure distributions on the airfoil at two x/c stations. The wake velocity vectors field (v & w) is measured using the 7HP data and the longitudinal vortex field ($\bar{\omega}_x$) is calculated using the velocity vectors. The spanwise pressure distribution is measured with the two pressure-taps rows as seen in Figure 6. Figure 25 presents the measurements for representative tests at 10° AoA and U_∞ = 25 [m/s] (Re = 6.4×10⁵).

The baseline case (Figure 25, left) presents four clear vortices that persist when actuation is added (Figure 25, center and right), these vortices may be the downstream development of the vortices emanating from the changes in cross-section geometry. The bottom charts in Figure 25 show the aft spanwise pressure distributions are almost constant when compared to the forward spanwise pressure distributions. The forward spanwise pressure distribution shows a gradient on both sides of the wing that peaks and plateaus where the nacelle and slat-cut out are located.

Closely examining the difference between the 3 test cases in Figure 25, it is observed that as the actuation magnitude is increased a counter-clockwise vortex appears between the 4 baseline vortices causing them to shift slightly. The effect of the actuation on the spanwise pressure distributions is apparent in the immediate vicinity of the actuators. Namely, in the forward row of pressure taps, around Y≈-0.08 coordinate a sharp pressure gradient appears as the actuation magnitude is increased.

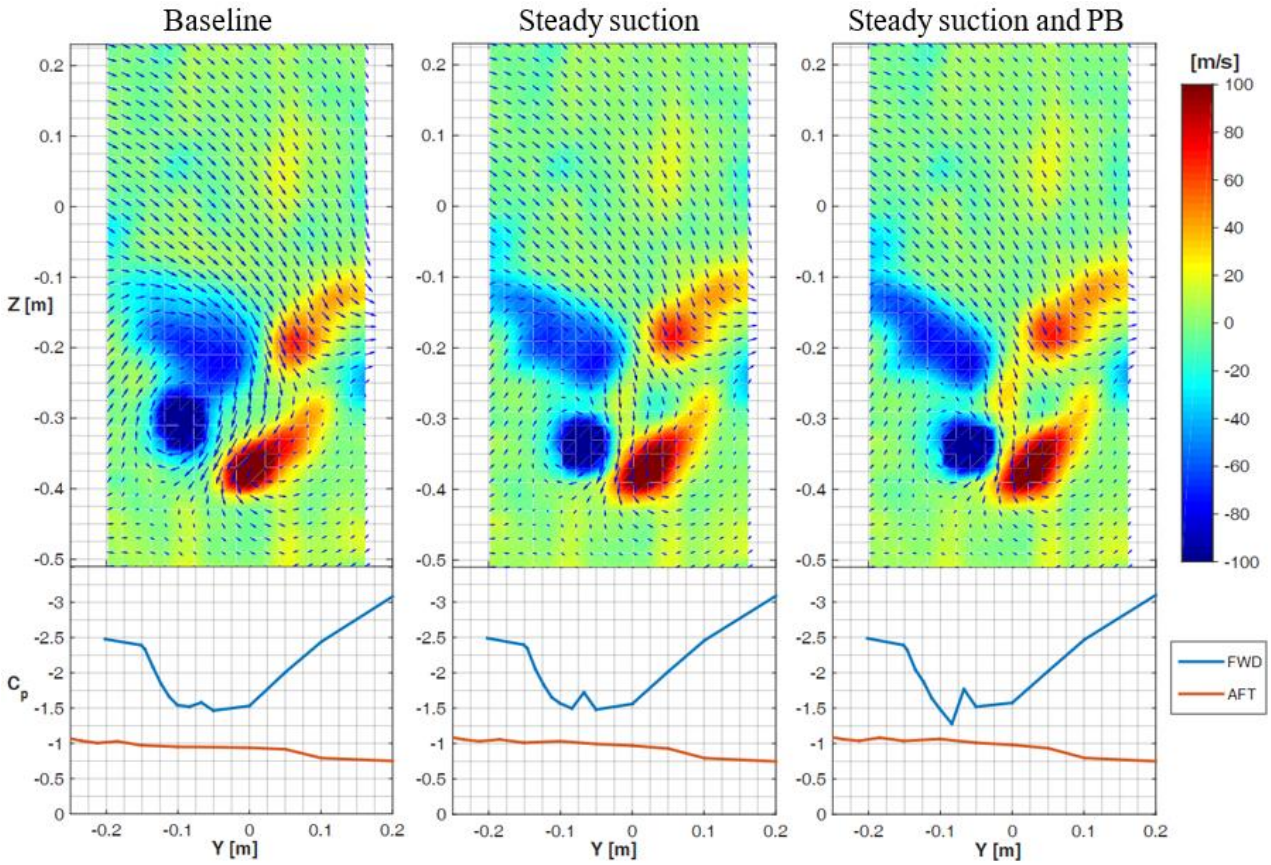

Figure 24. Y-Z velocity vectors (blue arrows, top) and longitudinal vortices wake-scan (color map, top) and C_p distributions along the two spanwise pressure tap rows (bottom) for 3 test cases: baseline flow (left), steady suction (center), steady suction and PB (right). AoA = 10°, U_∞ = 25 [m/s] (Re = 6.4×10^5), suction magnitude of C_μ = 3.1×10^{-3}, PB magnitude of C_q = 2.4×10^{-4} (VR =2).

4. CONCLUSIONS

A small-scale experimental study of an innovative active flow control device installed on a wing-engine-slat-cut out junction model is presented. This study is part of the EU Cleansky 2 INAFLOWT project where few CFD partners and large-scale WT tests are also conducted. The goal is to reduce detrimental flow effects of the coupling between the engine-wing-slat cut-out of this geometry, incorporating a large diameter engine in close proximity to the wing high-lift system. The study makes use of steady suction and pulsed blowing implemented at the leading-edge region of the wing above the nacelle, where a wide slat cut-out exists. The parameter study shows the positive effects of steady suction, applied at about 1.5% chord on the lift coefficient and the added contribution of the pulsed blowing mechanism, implemented at about 10%c, on maintaining the flow attached, where it separated.

With the goal of lowering the AFC mass-flow requirements, the effect of a reduced number of actuators is examined, and it is determined that the most effective area for actuation is from the inboard slat edge, towards the pylon, and up to, but not including, the nacelle's pylon. This is supported by surface oil flow visualization showing the reattachment of the flow in the separated area due to actuation, contributing to the understanding of the development of complex flow structures on this geometry. The evolution of longitudinal vortices is also examined and a link between the effect of the actuation, spanwise pressure gradient and a longitudinal vortex is established.

It is shown that as a result of the location of pressure sensors, the current method for evaluating the lift coefficient is under-estimating the changes in lift caused by actuation. Nonetheless, a 2.5-3% improvement in lift coefficient is achieved for most test cases of steady suction and pulsed blowing combined. The effect of actuation magnitudes and actuators' location on the flow structures is established parametrically for use in future near-full-scale experiments and industrial applications.

Future studies involving large scale experiments planned for the INAFLOWT project will benefit from the current study in several aspects:

- The future studies will use the results of this study to define the requirements of a full-scale SaOB device. This device will create suction using the ejector and using the sucked air to increase the PB mass flow. This will significantly reduce the required inlet mass-flow and yield a much higher energy efficiency

compared to pulsed blowing alone used to date.

- The full-scale tests will measure the lift coefficient using an integral force balance, creating a more accurate assessment of the AFC impact, alongside C_p measurements that can be directly compared to the current results.
- The AFC array of the full-scale tests will be installed in the most effective areas, found in this study, thus lowering the mass-flow requirements even further and compacting the system and its mass flux.
- Although drag reduction is not an official goal of this study, the drag can be measured more easily and precisely in the full-scale experiment. Potentially validating that the SaOB AFC also creates certain drag reduction benefits. Even in the current, locally separated flow case.

ACKNOWLEDGMENTS

The study was supported by a grant from the EU commission CS2 JU under project INAFLOWT, grant # 754307. The project is coordinated by Avraham Seifert and monitored by Bruno Stefes.

This presentation was partially supported by The Yakov Benveniste Student Travel Grant of Tel Aviv University

REFERENCES

1. Daggett, D. L., Brown, S. T., & Kawai, R. T. (2003). Ultra-efficient engine diameter study. NASA/CR—2003-212309.
2. Guynn, M. D., Berton, J. J., Fisher, K. L., Haller, W. J., Tong, M. T., & Thurman, D. R. (2011). Refined exploration of turbofan design options for an advanced single-aisle transport. NASA/TM–2011-216883.
3. Ullah, J., Prachar, A., Smid, M., Seifert, A., Soudakov, V., Lutz, T. & Kramer, E. (2019, March). Reynolds Number and Wind Tunnel Wall Effects on the Flow Field Around a Generic UHBR Engine High-Lift Configuration, 54th 3AF International Conference.
4. Lengers, M. (2014, September). Industrial assessment of overall aircraft driven local active flow control. In Proceedings of the 29th Congress of the International Council of the Aeronautical Sciences, St. Petersburg, Russia (pp. 7-12).
5. Schloesser, P., Soudakov, V., Bauer, M., & Wild, J. (2018). Active Separation Control at the Pylon-Wing Junction of a Real-Scale Model. *AIAA Journal*, 57(1), 132-141.
6. Rudnik, R. (2008). Stall behaviour of the EUROLIFT high lift configurations. In 46th AIAA Aerospace Sciences Meeting and Exhibit. AIAA 2008-836.
7. Schade, N. & v. Geyr, Heiko (2010). CFD Prediction of Maximum Lift Effects on Realistic High-Lift-Commercial-Aircraft-Configurations within the European project EUROLIFT II. Second Symposium "Simulation of Wing and Nacelle Stall", June 22nd - 23rd, 2010, Braunschweig.
8. Hue, D., François, C., Dandois, J., & Gebhardt, A. (2017). Simulations of an aircraft with constant and pulsed blowing flow control at the engine/wing junction. *Aerospace Science and Technology*, 69, 659-673.
9. Ullah, J., Monat, S., Seifert, A., Lutz, T. & Krämer, E. Active Flow Separation Control on a Generic UHBR Engine High-Lift Configuration by Means of Suction and Oscillatory Blowing, Notes on Numerical Fluid Mechanics and Multidisciplinary Design (Proceedings of SFB880 Final Symposium 2019), Springer, Germany 2020 (submitted).
10. Kato, H., Watanabe, S., Murayama, M., Yokokawa, Y., & Ito, T. (2008). PIV investigation of nacelle chine effects on high-lift system performance. In 46th AIAA Aerospace Sciences Meeting and Exhibit. AIAA 2008-240.
11. Cattafesta III, L. N., & Sheplak, M. (2011). Actuators for active flow control. *Annual Review of Fluid Mechanics*, 43, 247-272.
12. Greenblatt, D., & Wygnanski, I. J. (2000). The control of flow separation by periodic excitation. *Progress in aerospace Sciences*, 36(7), 487-545
13. Seifert, A., Darabi, A., & Wyganski, I. (1996). Delay of airfoil stall by periodic excitation. *Journal of aircraft*, 33(4), 691-698.
14. Sarkorov, D., Seifert, A., Detinis, I., Bauminger, S., & Steinbuch, M. (2016). Active flow control and part-span slat interactions. *AIAA Journal*, 54(3), 1095-1106.
15. Dolgopyat, D., & Seifert, A. (2018). Active flow control virtual maneuvering system applied to conventional airfoil. *AIAA Journal*, 57(1), 72-89.
16. Cordis, AFLoNext. https://cordis.europa.eu/project/id/604013/reporting. [Online; accessed 21-December-2019].
17. Schlösser, P., Bauer, M. Design of a pulsed jet actuator for separation control. CEAS Aeronaut J (2018) doi:10.1007/s13272-018-0328-x.
18. TAU, INAFLOWT, http://web.eng.tau.ac.il/~seifert/inaflowt. [Online; accessed 21-December-2019].
19. Cordis, INAFLOWT. https://cordis.europa.eu/project/id/754307. [Online; accessed 21-December-2019].
20. Arwatz, G., Fono, I., & Seifert, A. (2008).

Suction and oscillatory blowing actuator modeling and validation. *AIAA Journal*, 46(5), 1107-1117.

21. Prachar, A., & Vrchota, P. (2018). Characterization of the Suction-and-Oscillatory-Blowing actuator by the hybrid RANS-LES CFD. In 2018 Flow Control Conference (p. 3375).
22. Mizrahi, B., & Seifert, A. (2020, Fabruary). Development, Characteristic and Implementation of Oscillatory Suction Actuator for Boundary Layer Control. submitted for publication Aerospace Europe Conference AEC2020.
23. Vrchota, P. (2016). Application of Synthetic Jets Actuators in Wing-Pylon Junction Area to Improve the High Lift Performances. 10.7712/100016.2273.15461.
24. Vrchota, P. & Prachar, A. (2017). Active flow separation control applied at wing-pylon junction of a wing section in landing configuration. In 55th AIAA Aerospace Sciences Meeting. AIAA 2017-0491.
25. Fricke, S., Ciobaca, V., Kröhnert, A., Wild, J., & Blesbois, O. (2015). Active flow control applied at the engine-wing junction. In 5th CEAS Air and Space Conference (pp. 7-9). Netherlands: Delft.
26. Wild, J. (2013). Mach and Reynolds number dependencies of the stall behavior of high-lift wing-sections. *Journal of Aircraft*, 50(4), 1202-1216.
27. Gerner, A. A., Maurer, C. L., & Gallington, R. W. (1984). Non-nulling seven-hole probes for high angle flow measurement. *Experiments in Fluids*, 2(2), 95-103.
28. Ericksen, A. L., Gallington, R. W., Rao, B. M., & Barankiewicz, W. S. (1995). Rapid calibration of seven-hole probes. *NASA Technical Memorandum* 107040.
29. GitHub, Seven-Hole Probe Calibration. https://github.com/arielya/SevenHoleProbe/blob/master/Seven_Hole_Probe_Calibration.ipynb. [Online; accessed 21-December-2019].
30. Van Dam, C. P. (1999). Recent experience with different methods of drag prediction. *Progress in Aerospace Sciences*, 35(8), 751-798.
31. Giles, M. B., & Cummings, R. M. (1999). Wake integration for three-dimensional flowfield computations: theoretical development. *Journal of aircraft*, 36(2), 357-365.